

**Testing Dynamic Thermal Compensation of Optics
for Use in LIGO II**

by

Phil Marfuta

Submitted to the Department of Physics
in partial fulfillment of the requirements for the degree of

Bachelor of Science in Physics

at the

MASSACHUSETTS INSTITUTE OF TECHNOLOGY

June 2001

© Phil Marfuta, MMI. All rights reserved.

The author hereby grants to MIT permission to reproduce and
distribute publicly paper and electronic copies of this thesis document
in whole or in part.

Author
Department of Physics
May 11, 2001

Certified by.....
Rainer Weiss
Professor of Physics
Thesis Supervisor

Accepted by.....
Prof. David Pritchard
Chairman, Senior Thesis Coordinator, Department of Physics

Abstract

The Laser Interferometer Gravitational-wave Observatory (LIGO) is being built to directly observe and explore the astrophysical sources of gravitational radiation, a phenomenon predicted by General Relativity. The apparatus uses a 4 kilometer Michelson interferometer with Fabry-Perot arm cavities to detect phase shifts in laser light induced by a passing gravitational wave. Asymmetric power absorption in the interferometer's optics results in wavefront distortions in the laser beam, excessive losses in circulating laser power, leading to limitations on sensitivity. These distortions, as well as others introduced from other imperfections in the optical chain, can be represented by decomposing a phasemap measurement of the test mass into a set of orthogonal Zernike polynomials. Using a preexisting model, the Zernike decomposition can be used to determine how a CO_2 laser can selectively heat the optic to compensate for the optical distortion.

0.1 Acknowledgments

I would like to thank my family for their seemingly endless support; especially my mother, who used to tell me about black holes when I was a kid.

I am in debt to my compatriot, Ryan Landfield, for the competition and inspiration that only a best friend and fellow physicist can provide.

My gratitude also goes to Dr. TK McCarthy, aka “Doc”, for giving me a headstart on Quantum Mechanics and Special Relativity in high school, as well as breathing down my neck when I tried to slack off.

Thanks to Ryan Lawrence for patiently answering my questions while making fun of me.

The support of the members of the Theta Deuteron Charge of Theta Delta Chi was instrumental in keeping me sane and entertained for these four years.

Gracias to Professor Rainer Weiss, for being a really interesting person, as well as being a physicist a young guy can admire.

I am grateful for all of the little things Megan Owens helped with in this thesis, as well as her wonderful companionship.

I'd like to thank myself last, mostly because I think I'm a swell guy.

Contents

0.1	Acknowledgments	3
1	Introduction	8
2	LIGO	10
2.1	Design and Configuration	10
2.2	Sensitivity Limitations of LIGO	12
2.2.1	Seismic Noise: 10Hz-100Hz	13
2.2.2	Thermal Noise: 100Hz-300Hz	13
2.2.3	Shot Noise: 300Hz-2kHz	14
3	Underlying Principles	15
3.1	Linearity of Power Absorption	15
3.1.1	Heat Equation	15
3.1.2	Boundary Conditions	17
3.2	Zernike Functions	17
4	Dynamic Thermal Compensation	19
4.1	Theory	19
4.2	Implementation and Experimental Setup	21
5	Experimental Results	25
5.1	Data	26
5.2	Data Analysis	27

6	Conclusions	30
.1	Selected Zernike Functions	32
.2	LabView Control VI Explanation	33
.3	Data	43

List of Figures

2-1	An example of a delay line and Fabry-Perot interferometer	11
2-2	The Layout of LIGO II	12
4-1	Experimental Setup	23
-1	Wavefront form of $N = 4, 5, 8$ and 10	44
-2	Data for $N = 4, 5$ and 6	45
-3	Data for $N = 7, 8$ and 9	46
-4	Data for $N = 10, 11$ and 12	47
-5	Data figures	48

List of Tables

1	The first 15 Zernike Functions	32
---	--	----

Chapter 1

Introduction

Einstein's theory of general relativity predicts the existence of gravitational waves, ripples in the curvature of spacetime, propagating at the speed of light. Gravitational waves are radiated from all massive objects with a time varying quadrupole moment, although they are weak enough in interaction to have avoided direct detection thus far. Despite their faintness, gravitational waves cannot be easily attenuated or scattered and can therefore provide an undistorted observation of the properties of large accelerating astronomical objects. Besides verifying an aspect of Einstein's popular theory, detection of gravitational waves could give information about the characteristics of their propagation, details of strong gravitational interactions and could pick up residual gravitational noise from the primeval universe.

Gravitational waves interact with mass by producing a quadrupolar strain along two axes transverse to their propagation. The path length between two free masses along these axes would experience a change in magnitude as the gravitational wave passes. For this reason several variants of a Michelson interferometer have been suggested as ways to detect gravitational waves.

LIGO is one such project consisting of two 4 km long interferometric detectors run in coincidence; one is in Hanford, WA and the other in Livingston, LA. The LIGO design also incorporates Fabry-Perot cavities in each arm and a power recycling mirror between the input laser and the beamsplitter. LIGO is expected to be able to detect a strain of $h = 10^{-21}$ at 100Hz which would result in a path length change

of $\delta L = 10^{-18}m/\sqrt{Hz}$ and therefore an optical phase lag of $\delta\phi = 10^{-10}rad/\sqrt{Hz}$ at the beamsplitter, producing photons at the antisymmetric port. LIGO II will consist of upgrades to the original equipment which will increase the broadband strain sensitivity by a factor of 10 to 15.

LIGO's sensitivity is primarily limited by three main factors: seismic noise due to motion of the ground (10-100Hz), thermal noise produced by Brownian motion of the mirrors and test masses (100-300Hz), and shot noise due to photon counting statistics (300Hz-2kHz). Upgrades in the seismic isolation systems for the test masses and a change to mirrors and suspension materials which have low internal losses will respectively improve the noise limit caused by the first two sources. Photon counting statistics can be improved by increasing the power circulating in the apparatus. Ideally one could use a sufficiently powerful laser to lower this limit as much as needed, but increasing the power produces larger fluctuations in the radiation pressure, which becomes an important noise limit in LIGO II. The combination of shot noise and radiation pressure noise comprises a locus of lowest possible noise known as the "quantum limit". Some improvement is possible in LIGO II by increasing the power recycling in the interferometer. At this higher power, heating of the optics due to power absorption becomes important. As a result of this heating, mechanical deformations can occur on the surface of the optics, termed "thermoelastic deformation". This, as well as the temperature dependence of the index of refraction of the optics, called "thermal lensing", imposes additional limitations on the power which can be used.

Thermo-optical effects in LIGO II's optics can be addressed by a combination of static and dynamic corrective measures. The static technique involves using a shielded current carrying coil of nichrome filament to radiate heat onto the flat face of the optic to remove gross axially symmetric heating nonuniformities. The active technique is the focus of this thesis, and it will be used to correct residual, possibly non-axisymmetric nonuniformities. It will involve a closed loop system that continuously checks the optic for wavefront deformations and corrects them by scanning a CO_2 laser across the face, depositing heat on the surface in such a way as to make the wavefront uniform.

Chapter 2

LIGO

The Laser Interferometer Gravitational Wave Observatory, or LIGO, is a ground-based observatory which measures phase shifts in laser light to detect and record the properties of a passing gravitational wave. Interferometric gravitational wave detectors have advantages over their bar-detector predecessors in that they can detect more than a single frequency of gravitational wave as well as obtaining high sensitivity. LIGO will be able to detect gravitational waves from astronomical phenomena such as supernovas and binary star systems with frequencies between 10-2000 Hz at a dimensionless strain of $h = 10^{-21}$ or less.

2.1 Design and Configuration

The fact that a passing gravitational wave produces a transverse differential strain makes a Michelson interferometer a good detector due to its sensitivity to differential length changes in its arms. A Michelson interferometer has constructive interference in the symmetric port where the laser light enters, and completely destructive interference at its antisymmetric or “dark” port until a change in path length destroys the interference, resulting in light detected at the dark port. Since gravitational waves produce a strain, the change in pathlength produces a time delay in photon arrival time; for this reason longer interferometer arms improve sensitivity by increasing the interaction time of the gravitational wave with the light. One way to increase beam

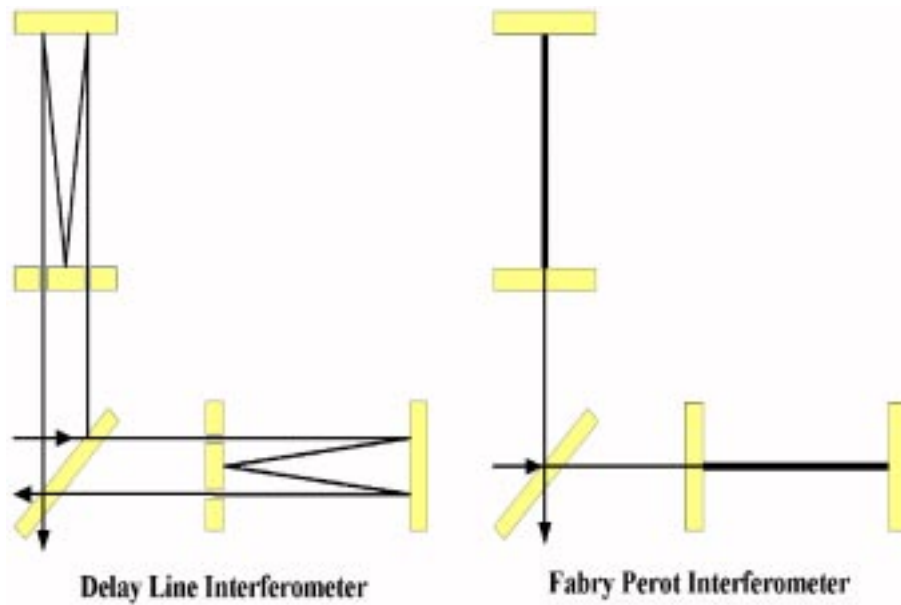


Figure 2-1: An example of a delay line and Fabry-Perot interferometer [7]

path length is to fold the beam over several times by modifying the interferometer design. This is done in LIGO with a Fabry-Perot interferometer, primarily because LIGO uses compact geometry (small mirrors and beams) and a Fabry-Perot interferometer allows for smaller mirrors than other alternatives. Other designs can be used as well - one such design is a delay-line interferometer. Figure 2-1 shows the schematic differences between these two examples. One can see a Fabry-Perot interferometer requires small mirrors because the beam hits the same spot on each mirror with each bounce.

When the interferometer interacts with a gravitational wave, the light in the arms accumulates a phase shift. The additional bounces increase the time of interaction between the light and the wave. This produces a larger phase shift and a stronger signal, which has a maximum when the arm cavity storage time is equal to one half of the gravitational wave period. However, additional bounces result in additional power losses due to imperfections in the optics as well as an increased coupling to thermal and seismic motions of the test masses. Increasing the length of the interferometer

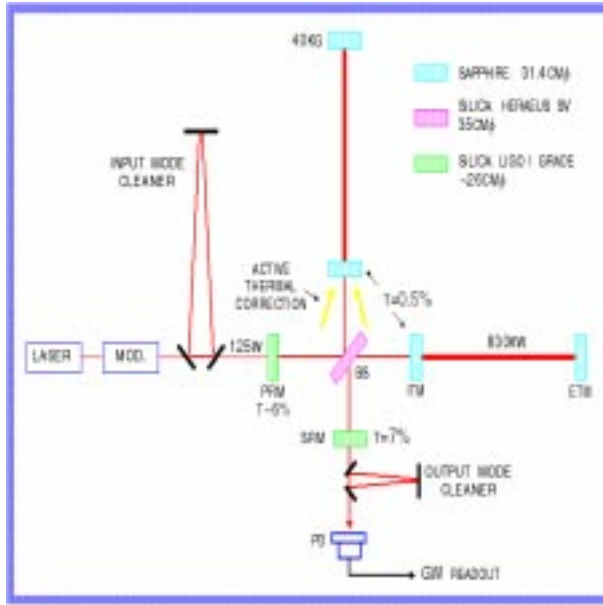


Figure 2-2: The Layout of LIGO II

arms reduces most important sources of noise by reducing the number of bounces required for a given path-length. Additionally, few sources of noise grow stronger with an increased arm length. LIGO's arms were made to be 4km long.

Larger signals can be generated by increasing the amount of power incident upon the beam splitter, since this translates into a higher intensity at the dark port when a gravitational wave passes. For this reason LIGO includes a power recycling mirror between the laser and the beamsplitter which is equivalent to using a higher power laser. The setup of LIGO II is shown in figure 2-2. This figure differs from LIGO in that LIGO does not have an amplitude recycling mirror and an output mode cleaner at the dark port, has only fused silica optics and has no thermal correction.

2.2 Sensitivity Limitations of LIGO

LIGO II should have improvements that will increase the $h = 10^{-21}$ sensitivity by a factor of 10. LIGO II is designed to be very likely to detect the coalescence of neutron star/neutron star binaries, and depending on their uncertain abundance,

also very likely to observe black hole/compact object binaries. LIGO II will also be broadband enough to detect unexpected sources of gravitational radiation. In order to achieve this level of sensitivity, LIGO must undergo improvements.

2.2.1 Seismic Noise: 10Hz-100Hz

Seismic noise in LIGO is dealt with by a combination of active and passive techniques. Passive techniques include isolation stacks for all of the optical equipment as well as hanging the test masses from thin wire with a pendulum frequency of about 1 Hz, outside of the gravity wave band observable by LIGO. LIGO II components may be mounted from an active isolation system, while the test masses may hang from multiple pendula.

2.2.2 Thermal Noise: 100Hz-300Hz

Thermal noise in the optics, test masses and optical mounts can be reduced by choosing materials with low internal loss. Presently the material of the test masses is fused silica (SiO_2), which may be changed to sapphire (Al_2O_3) for its lower internal loss. This internal loss is the dominant source of noise for fused silica. Sapphire has a crystalline structure and therefore lower internal loss. It also has a higher thermal conductivity, allowing it to handle more laser power. However, it also has a higher coefficient of thermal expansion, which could lead to more thermo-optic distortions than in fused silica. Additionally, the higher coefficient of thermal expansion results in more thermoelastic noise than in fused silica; here “thermoelastic noise” is used to describe the result of small scale thermodynamic fluctuations of an object at a uniform average temperature. These fluctuations in temperature produce fluctuations in position measurements of the surface. Uncertainties in the position measurements of the optics lead to noise in the interferometer which could potentially drown out the change in differential arm length induced by a gravitational wave.

2.2.3 Shot Noise: 300Hz-2kHz

Shot noise limits the sensitivity due to the Poisson statistics of photon arrival. The shot noise varies as \sqrt{P} with power, while the signal goes linearly with power. The signal to noise ratio therefore goes as $1/\sqrt{P}$, and shot noise is reduced with increased power [2]. As the power circulating in the arms increases the amount of power lost increases. The dominant source of this power loss is due to scattering, although absorption of light by the optics contributes slightly. The interferometer has been designed so that the recycling mirror has a transmission of 3%, which accounts for all of the losses in the entire interferometer. In LIGO I there is an input laser power of 8 Watts, a recycling gain of 30 and an arm cavity finesse of 200, and in LIGO II this will be increased to an input laser power of 180 Watts, a recycling gain of 30 and an arm finesse of 1000. It is estimated that an average power of 25mW will be absorbed by the fused silica optics in LIGO I, and 0.5 Watts for fused silica and 7.0 Watts for sapphire optics in LIGO II [4].

This larger amount of power absorption in LIGO II leads to a level of thermo-optical deformation which must be compensated for. Additionally, the index of refraction of the optic varies with temperature, which thermally distorts the wavefront of the reflected or transmitted light. Nonspherical deformations result in additional power being scattered out of the fundamental mode of the cavity, resulting in a loss of power recycling through the interferometer. This effect can be corrected by using a combination of passive and active corrective techniques, the latter of which is the focus of this thesis [4].

Chapter 3

Underlying Principles

A knowledge of the Heat Equation and of Zernike Functions will prove useful in this experiment.

3.1 Linearity of Power Absorption

3.1.1 Heat Equation

The amount of thermal energy $Q(t)$ at time t contained in a three-dimensional body with volume V , given a temperature distribution $T(\vec{r})$, can be written:

$$Q(t) = \int \int \int_V c\rho T(\vec{r}, t) d\vec{r} \quad (3.1)$$

where $c = c(\vec{r})$ is the heat capacity and $\rho = \rho(\vec{r})$ is the mass density of the object.

Dynamically, we can write the change in thermal energy as:

$$\frac{dQ(t)}{dt} = \int \int \int_V c\rho \frac{\partial T(\vec{r}, t)}{\partial t} d\vec{r} \quad (3.2)$$

If $\frac{dQ(t)}{dt}$ is positive there is a net amount of energy deposited in the body. The

distribution of heat deposited per unit volume can be represented as $H(\vec{r}, t)$. Conservation of energy demands the change in thermal energy must be equal to the heat leaving through the surface of the volume V plus the net input energy due to the bulk heating H . The heat leaving through the surface can be found by applying Stoke's theorem to 3.2:

$$\frac{dQ(t)}{dt} = \int \int k(\vec{r})(\hat{n} \cdot \vec{\nabla}T(\vec{r}, t))dS + \int \int \int H(\vec{r}, t)d\vec{r} \quad (3.3)$$

where $k = k(\vec{r})$ is the thermal conductivity and \hat{n} is the unit vector normal to the surface. Applying the divergence theorem to 3.3 and equating it with 3.2, we see:

$$\int \int \int c\rho \frac{\partial T(\vec{r}, t)}{\partial t} d\vec{r} = \int \int \int H(\vec{r}, t) d\vec{r} + \int \int \int \vec{\nabla} \cdot (k(\vec{r}) \vec{\nabla} T(\vec{r}, t)) d\vec{r} \quad (3.4)$$

Now, since V is any arbitrary volume which all three terms are integrated over, we can equate the integrands alone. This gives us the Heat Equation:

$$\rho c \frac{\partial T(r, z; t)}{\delta t} - \vec{\nabla} \cdot (k(\vec{r}) \vec{\nabla} T(\vec{r}, t)) = H(\vec{r}, t) \quad (3.5)$$

In the case of heating with LIGO's main beam, we can exploit the cylindrical symmetry of the optic and assume the net bulk heating is steady-state. Therefore k , c , and ρ are constant over a cylindrically symmetric region V , $H(\vec{r}, t) = H(r)$, and $T(\vec{r}) = (r, z, \phi) = T(r, z)$. Now the previous equation becomes:

$$\begin{aligned} \rho c \frac{\partial T(r, z; t)}{\delta t} - H(r) &= k \left(\frac{1}{r} \frac{\partial}{\partial r} r \frac{\partial}{\partial r} + \frac{1}{r^2} \frac{\partial^2}{\partial \phi^2} + \frac{\partial^2}{\partial z^2} \right) T(r, z, t) \\ &= k \left(\frac{1}{r} \frac{\partial}{\partial r} r \frac{\partial}{\partial r} + \frac{\partial^2}{\partial z^2} \right) T(r, z, t) \\ &= \frac{1}{r} \vec{\nabla}_2 (kr \vec{\nabla}_2 T(r, z, t)) \end{aligned} \quad (3.6)$$

where we have written $\vec{\nabla}_2 \equiv \hat{r} \frac{\partial}{\partial r} + \hat{z} \frac{\partial}{\partial z}$. 3.6 now may be written as:

$$r\rho c \frac{\partial T(r, z; t)}{\delta t} - \vec{\nabla}_2(kr \vec{\nabla}_2 T(r, z, t)) = rH(r) \quad (3.7)$$

which is the Heat Equation for a closed surface in the right half plane with a density ρr , heat capacity c , and thermal conductivity kr .

3.1.2 Boundary Conditions

Assuming that the body is thermally isolated except for its interaction with a radiation bath of temperature T_∞ , we can approximate it as a blackbody and use the Stefan-Boltzmann law to define its boundary conditions:

$$\hat{n} \cdot (k \vec{\nabla} T) = -\sigma\epsilon(T - T_\infty)^4 + H(\vec{r}, t) \quad (3.8)$$

Here ϵ is the emissivity, and σ is the Stefan-Boltzmann constant. We can also assume that $\frac{T - T_\infty}{T_\infty} \ll 1$, which allows us to linearize the radiation term by writing:

$$\hat{n} \cdot (k \vec{\nabla} T) = -4\sigma\epsilon T_\infty^3 (T - T_\infty) + H(\vec{r}, t) \quad (3.9)$$

The linearity of both the heat equation and the boundary condition above ensure linearity in the power absorbed by the body.

3.2 Zernike Functions

Zernike Functions are orthogonal and are complete on the unit circle. Due to their cylindrical symmetry and finite radial boundaries, they are ideal for describing wave-front distortions in optics. In practice one can reduce the radius of the modeled optic

by dividing by a scale factor, fit Zernike functions to the unit circle, and then multiply by the scale factor to produce the actual fit. The functions are defined by:

$$Z_n^l(r, \phi) = R_n^l(r) \cdot \Phi(m, \phi) \quad (3.10)$$

where $m \equiv \frac{n-l}{2}$, $\Phi(m) = \sin m\phi$ if l is odd or $\Phi(m) = \cos m\phi$ if l is even. $R_n^l(r)$ are known as Zernike Polynomials, and are defined by the relation:

$$R_n^l(r) = \sum_{j=0}^m \frac{(-1)^j (n-j)!}{j!(n-m-j)!(m-j)!} r^{n-2j} \quad (3.11)$$

Zernike functions are orthogonal with the relation:

$$\int_0^{2\pi} \int_0^1 Z_n^l Z_{n'}^{l'} dr = \frac{\pi \epsilon_{nm}}{2(n+1)} \delta_{mm'} \delta_{nn'} \quad (3.12)$$

where ϵ_{mn} is equal to 2 when $l = 0$ and equal to 1 otherwise. Zernike functions are also frequently referred to by their order or number. The number of the Zernike polynomial is then $N = n(n+1)/2 + m + 1$. Table 1 (Appendix 1) contains the first 15 Zernike functions in their polar and rectangular form along with the common name associated with some of them [5]. It should be noted that as N increases, the Zernike functions have more ‘lobes’ both in the radial and tangential direction when graphed on a polar grid; therefore higher order Zernike functions require more resolution to measure or reproduce.

Chapter 4

Dynamic Thermal Compensation

Absorption of power from a laser occurs in even the most efficient optics. This and the radial dependence of beam intensity lead to thermal lensing for two reasons: first, the index of refraction varies uniformly with temperature; second, there is nonuniform thermal expansion of the optic. We can counteract these effects by continuously monitoring the wavefront distortion due to the optic and render it flat by depositing heat on the optic's surface according to a model of the optic.

4.1 Theory

Assuming a temperature field which varies radially and axially in a cylindrical optic, $T(r, z)$, we can write the optical path length $\phi_t(r)$ through the optic as:

$$\phi_t(r) = \int_0^{h(r)} n(r, z) dz \quad (4.1)$$

$$\simeq n_0 h_0 + \frac{dn}{dT} \int_0^{h_0} (T(r, z) - T_\infty) dz + n_0 (h(r) - h_0) \quad (4.2)$$

$$= \phi_{t0} + \phi_{tl}(r) + n_0 \Delta h(r) \quad (4.3)$$

Here $n(r, z)$ is the index of refraction of the optic with n_0 being its nominal value, $h(r)$ is the displacement of the surface due to thermal expansion with h_0 as its nominal value and the thermoelastic deformation of $\Delta h(r) \equiv h(r) - h_0$, $\phi_{tl}(r)$ is the optical

path distortion due to thermal lensing with an undistorted optical path of ϕ_{t0} . For reflections off the face, we can write:

$$\phi_r(r) = \phi_{r0} - s\Delta h(r) \quad (4.4)$$

We can then use a finite element model to calculate the temperature field, utilizing the linearity of the boundary conditions as previously discussed, and use this to calculate the optical path length change due to the temperature field. We can also use another finite element model to determine the vector field of deformations given the temperature field.

The different times of arrival for a single monochromatic light pulse, due to variations in the optical path length $\phi(r)$, result in a phase lag at different points. The optical path length can therefore be viewed as a map of the wavefront from the optic. This phasemap, $\phi(r, \theta)$, can be measured on a polar grid and decomposed into constituent Zernike functions:

$$\phi(r, \theta) = \sum_{j=1}^N A_j Z_j(r, \theta) \quad (4.5)$$

We can then use a numerical model to determine the effect on the wavefront when a laser with known parameters scans across a constant grid of points on the optical face, producing optical distortions via heat deposited on the optic. Suppose the scanning pattern shines the correcting Gaussian laser beam of waist w_a :

$$I(\vec{r}) = \frac{2P_m}{\pi w_a^2} e^{-2\frac{(\vec{r}-r_m)^2}{w_a^2}} \quad (4.6)$$

over a discrete grid containing M points, indexed by m . We wish to obtain the M -dimensional power matrix \mathbf{P} to induce the N dimensional Zernike decomposition \mathbf{Z} . To do this, we find the $M \times N$ matrix known as the actuation operator \mathbf{O} such that

$$\mathbf{P} = \mathbf{O} \cdot \mathbf{Z}.$$

If we shine the laser on the m th grid point we can either measure or calculate the steady state phase distortion ϕ_m . ϕ_m can be decomposed into Zernike functions such that $\sum_1^N a_{nm}Z_n$. If we do this for each of the M points, the coefficients a_{nm} make up an $N \times M$ matrix \mathbf{a} which allows us to determine the wavefront distortion \mathbf{Z} , given a power vector \mathbf{P} : $\mathbf{Z} = \mathbf{a} \cdot \mathbf{P}$. It follows that the actuation matrix \mathbf{O} is the inverse of matrix \mathbf{a} [1].

We can constantly monitor the wavefront distortion, $\phi(r, \theta)$, on the optic and from it determine $\mathbf{A}_{\text{optic}}$. We can introduce an additional wavefront curvature, $\phi_c(r, \theta) = B - \phi(r, \theta)$, to produce any arbitrary wavefront form, B , that we wish. By choosing a matrix \mathbf{B} with constant elements such that the required laser power is a minimum, we can obtain our desired $\mathbf{A} = \mathbf{B} - \mathbf{A}_{\text{optic}}$. We then invert \mathbf{a} by single value decomposition to obtain our desired actuation matrix \mathbf{O} and multiply it by \mathbf{A} to get the required power at each of the M points to render the wavefront flat.

4.2 Implementation and Experimental Setup

We found from our modeling that a scanning pattern consisting of 10 concentric circles (including the center point) with each circle containing 17 points along the perimeter (154 points total) would yield the smoothest heating distribution. Higher order Zernike functions require higher resolution to produce, and because of limitations in resolution available to us due to the size of the CO_2 beam and spreading due to thermal diffusion, there is a limitation to the number of Zernike functions we could consider for our model. In our case it was practical to consider only the first 36 Zernike functions because any more would require a larger input power than we had available.

The final version of the model was obtained by heating each of the ten points along the x-axis separately with an RMS power of $94mW$, allowing the optic to reach thermal equilibrium, and then observing the magnitude of excited Zernike coefficients, which is equivalent to measuring the magnitude of the optical path distortion. The

response to the ten points could be loaded into Matlab where we were able to rotate the illuminated points about the center, producing the response for all 154 points individually. We cataloged this response with a 36×154 matrix \mathbf{a} . When inverted and multiplied on the right by the 36×1 matrix \mathbf{Z} containing 36 Zernike coefficients, the result is the 154×1 matrix \mathbf{P} . Therefore, by choosing the 1×36 matrix \mathbf{Z} to have all elements equal to 0 except for a value of 1 on the Nth element, we can expect the result to be the power needed at each point on the grid in order to make the wavefront into the Nth Zernike polynomial.

Figure 4-1 shows our experimental setup. The probe beam reflects from the test optic, feeding part of the beam into a wavefront sensor in order to measure wavefront distortions. To correct the distortions, a CO_2 laser is scanned across the face of the optic by two galvanometers and its intensity is controlled by an acousto-optic modulator.

Our cylindrical fused silica optic is $10cm$ in diameter and $8cm$ deep. We keep it in a vacuum chamber of about 10^{-7} torr.

We use a $\lambda = 633nm$ fiber pigtailed laser diode, expanded to the size of the test optic, as the probe beam. The reflected beam is sent back through the optical chain, with a polarizing pick-off diverting some of the power into a wavefront sensor.

Our wavefront sensor is a commercially available Shack-Hartmann sensor which consists of a two-dimensional cylindrical lenslet array. The lenslets break up a distorted beam into a number of facets which create a focus on the focal plane of the detector. The average wavefront over the lenslet aperture determines the position of the focal spot. Thus the local wavefront slope can be determined by the relative position of the focal points on the focal plane.

We used a $10W, \lambda = 10.6\mu m CO_2$ laser to illuminate the test optic in order to thermally actuate the test optic, thereby inducing the desired distortions in the wavefront of the probe beam. The laser came from the manufacturer with $\pm 10\%$ power stability, but we used a thermopile to form a servo loop which steadied the intensity to 3% of the mean.

We used two galvanometers to control position of the CO_2 beam on the optic, one

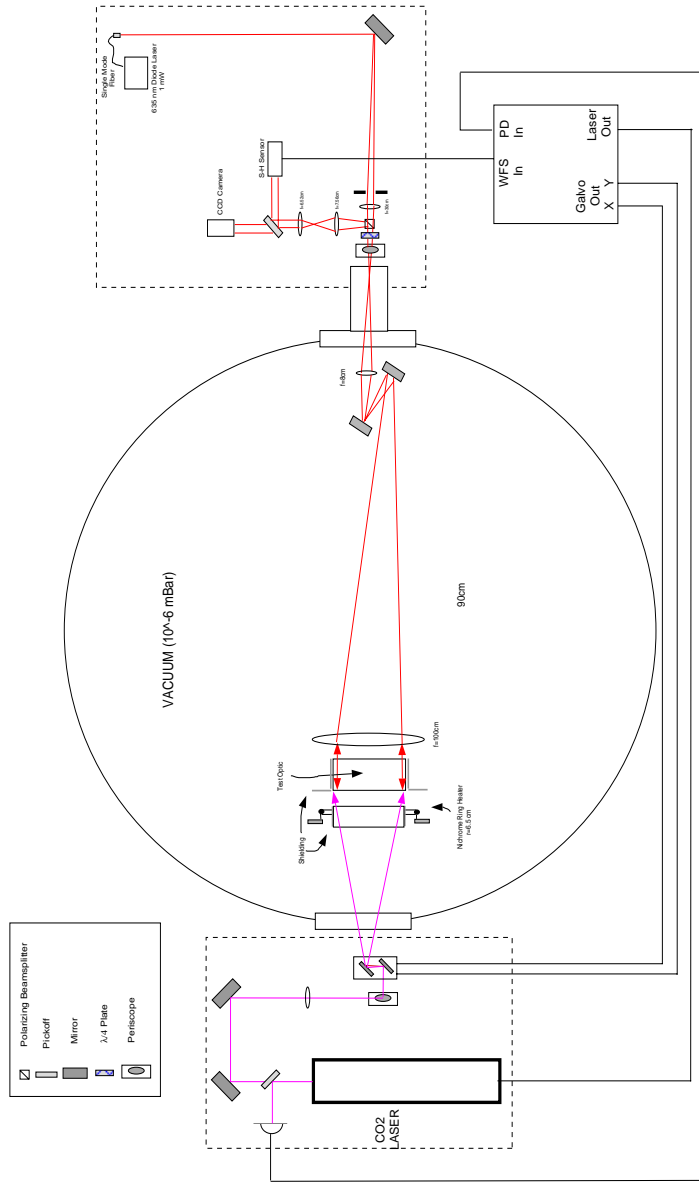


Figure 4-1: Experimental Setup
[4]

oriented for vertical displacement, the other for horizontal. They are high-speed, high-precision devices capable of handling our scanning speeds of 50 points/*ms*.

Our laser cannot be modulated any faster than 1*KHz*, so we use an acousto-optic modulator (AOM) to modulate the laser intensity at the required 4*KHz*. The AOM uses an RF frequency acoustic wave propagating in an optically transparent medium to produce a periodic change in the index of refraction. This periodic change produces a standing wave which acts as a grating capable of diffracting an incident laser beam. The Bragg angle, $\theta_B = \frac{\lambda}{2\Lambda}$, is half the angle between the undeflected transmitted beam and the first order diffracted beam, where λ is our optical wavelength of 10.6 μm and Λ is the acoustic wavelength of 13.8*mm*. The power delivered in the first order beam is related to the voltage applied to the AOM driver:

$$P = A \sin^2(B \cdot V) \tag{4.7}$$

where A and B are constants determined by our calibration. When no voltage is applied to the driver, we can achieve total extinction of the first order beam. According to the manufacturer, 90% of the incident beam's power can be diffracted into the first order. Therefore the first order beam is ideal for amplitude modulation.

My primary thesis work was the design and implementation of a LabView virtual instrument which controlled the galvanometers and AOM, dispersing the desired powers over the face of the optic. The details of this program are contained in Appendix.2, and the results are presented in the next chapter.

Chapter 5

Experimental Results

We performed an open loop test over a two week period in order to test the accuracy of our model and our control system. We wished to feed a particular Zernike coefficient to the control system and see how well it could duplicate that particular wavefront distortion. For each Zernike polynomial we tried to produce, we scaled the power at each point such that the point on the optic requiring the most power got the maximum of $2.2W$ we could introduce into the system. We were inducing the largest optical path distortion possible with our setup for each Zernike polynomial. Higher order (larger N) Zernike functions have more features than those of lower order. Since all Zernike functions are described on the same unit circle, the more peaks and troughs the Zernike polynomial has, the closer the peaks and valleys are together. This means the resolution required to measure or produce Zernike functions generally increases as N does. Since our laser is not an idealized point and heat on the surface of the optic spreads due to thermal diffusion, we can only achieve a limited resolution. This limitation on resolution manifests itself in two ways. First, as mentioned previously, our model only considered the first 36 Zernike functions; considering more would improve our ability to extinguish unwanted Zernike coefficients, but would require more laser power than we have available. Second, suppose we wish to create a Zernike polynomial with a coefficient of $1.0 \times 10^{-6}cm$. The laser power required to do this is greater for higher order Zernike functions. We are, however, limited to a $2.2W$ difference between the points on the grid requiring the most and

the least power. Therefore we expect to see a smaller amplitude of induced coefficients for higher order Zernike functions; even though we use the first 36 functions in our model, this does not mean we can reproduce all of them. The motivation of this experiment was to demonstrate the ability to generate a wavefront in the shape of a preselected Zernike polynomial, as well as to determine how many Zernikes could be generated before resolution and power limitations render the difference from background unmeasurable.

Eventually the experiment will be upgraded to a closed loop system where the LabView program sends a 10 volt TTL pulse to the wavefront sensor every 10 minutes, triggering it and causing it to write the Zernike decomposition to a text file. The text file is then read by Matlab and combined with information from the finite element model to obtain the power which needs to be deposited at each point. These powers are then converted into voltages to be sent to the AOM by Matlab, which uses a calibration conversion between power and voltage output. The result is written into a file by Matlab and read by LabView, which then uses the laser to render the wavefront as flat as possible before the next iteration.

5.1 Data

Our measurements went from the $N=4$ to the $N=13$ Zernike (see Appendix .1 for notation). The first Zernike, $N=1$, is piston (uniform wavefront) and is unmeasurable since the wavefront sensor only measures relative differences in the wavefront. $N=2$ and $N=3$ are tip and tilt in the X and Y direction, and are easily filtered out: they do not require thermal compensation to eliminate. Anything beyond $N=13$ was indistinguishable from noise.

After we selected the number Zernike we wished to induce, we heated the optic for approximately 20 minutes, the approximate time for the peak to valley wavefront distortion to become steady state. We then averaged 20 frames at three separate times after the initial 20 minute wait. We then let the optic cool for 20 minutes before averaging 20 frames at three separate times in order to determine what wave-

front distortions had occurred in the during the run. The peak to valley optical path distortion typically grew from a “flat” $2.0nm$ to $60nm$ over the time duration of one run, due to systematic and random drifts in the system. We could characterize these motions by doing a Zernike decomposition of the wavefront after each run. We then compared the contributions of different Zernike functions to the drift by averaging each Zernike coefficient over the 30 residual wavefronts we had measured. We then chose the standard deviation about that mean to be the ‘noise level’ for each Zernike polynomial. Any coefficient measured to be smaller than or on the order of this noise level was indistinguishable from the motions which occurred during the data run. For example, the largest contribution to the drift came from the $N=8$ Zernike polynomial, third order coma with its axis along the x-axis. Coma about an axis occurs naturally when a measurement is made off of that axis. Therefore we can conclude the largest part of the noise level comes from random horizontal walking of the table, the optic, or other optical components.

5.2 Data Analysis

Due to properties of the optic, our model was extremely sensitive to the $N=5$ Zernike polynomial, also known as focus. The actual result of the actuation basis discussed in section 4.1 is a matrix with both positive and negative entries: ideally one would add power to certain points and remove it from others. Due to the properties of the optic, depositing a constant power over the face of the optic does not exclusively produce the $N=1$ Zernike polynomial, piston, but rather adds higher terms, including focus, so one cannot simply add a constant power to each point, setting the point of least power equal to zero. It is challenging to render the negative powers positive, and involves a fix to the matrix based upon an approximation. In doing so, small uncertainties, even from the noise in our measurement of the optic’s response to the CO_2 beam, produce a larger focus term than the model predicts.

For a qualitative analysis, let us examine the images of the wavefront distortion, shown in .3. Lighter colors represent a greater optical path length. To begin with,

we have $N=5$, or focus, as shown in figure -1.

The $N=4$ and $N=6$ Zernike functions are astigmatism about a 45 degree and 90 degree axis, respectively. $N=4$ (figure -1) was the best data set we obtained. Note that the focus term had little effect.

$N=8$ and $N=9$ are coma about the x and y axes, respectively. Note the significant role focus has in the data shown in figure -1.

$N=7$ and $N=10$ are triangular astigmatism about the x and y axes, respectively. $N=10$ is displayed in figure -1.

For a more quantitative measurement, we plotted the actual Zernike coefficients from the wavefront decomposition for each data set along with the coefficients the model predicts. We also included the noise level in each figure. From these we could compare how well we could get the predicted and actual induced Zernike coefficients to agree, how well we could extinguish other Zernike functions, and how many Zernikes we could produce before our signal is drowned out by the noise, which had a peak to valley range of $\pm 4 \times 10^{-7} cm$. We will discuss some Zernike functions of interest here, but the complete set is in .3.

In figure .3, we can see the predicted and actual coefficients agree very strongly on a value of $4.05 \times 10^{-6} cm$. Note that the noise is a full order of magnitude smaller than the induced Zernike coefficient.

$N=5$ (shown in figure .3) also had good agreement with the model, although the induced coefficient has a magnitude of $2.05 \times 10^{-6} cm$, almost a factor of 2 smaller than that shown in figure .3.

$N=6$ (shown in figure .3) has a slight disagreement with the model; the measured $2.93 \times 10^{-6} cm$ value was smaller than the expected $3.41 \times 10^{-6} cm$. Also note the $N=5$ focus term has a measured value almost two orders of magnitude larger than the expected value.

By the time we reach $N=8$ (shown in figure .3), the focus term has become larger than the term we are seeking to induce. However, the model is in fairly good agreement with the measured value $7.03 \times 10^{-7} cm$. Note that this value is about the same order of magnitude as the peak to valley noise for the first time.

Finally, at $N=12$ (shown in figure .3), the measured value of $2.77 \times 10^{-7}cm$ becomes smaller than some of the noise terms. The model is still in fair agreement with the results on this value, although other terms seem to disagree greatly with the prediction.

We can also demonstrate the diminishing magnitude of the wavefront deformations with increasing number by plotting all the data runs on the same graph with the noise level. In figure .3, only the coefficients which we attempted to induce are shown. As expected, our signal diminishes as the number Zernike increases.

It is also useful to determine how the focus term changed as we tried to induce one Zernike polynomial to the next, as this may allow us to better understand how to fix the problem. Aside from the $N=5$ term shown in figure .3, which occurred when we were trying to create as large a focus term as possible, it seems that the magnitude of that coefficient changes little from data run to data run. This seems to support the hypothesis that the additional focus terms are a constant artifact of the model.

Chapter 6

Conclusions

The open loop test was a moderate success with room for improvement. The data conclusively shows thermally adaptive optics is possible, but a few difficulties need to be resolved before a closed-loop system can render the wavefront flat enough for use in LIGO.

Preliminary qualitative tests showed that perhaps as many as 200 Zernike functions need to be produced accurately in order to decompose and reconstruct a known wavefront deformation to within 1%. In order to accomplish this, a great increase in available laser power is needed. Possibilities include getting the AOM up to manufacturer specifications, which would boost the available power from 2.2W to around 9.0W. A larger CO_2 laser could also improve this.

Limitations in accuracy could also be the cause for the inability to extinguish coefficients other than the desired ones. Methods of improving this include a better stabilization of the CO_2 laser, better alignment of the probe beam with the heating beam on the center of the optic, and performing the Zernike decomposition of the raw wavefront data on Matlab rather than leaving it to the WFS software. Additionally, during the trial run where we observed the effect of the CO_2 beam on each of the 10 radial points, the wavefront sensor was not recalibrated between each point, resulting in noisy data. Improving this and understanding the source of the noise that occurs over 15 minute periods will allow us to create a more precise experimental model of the optic.

The ultimate goal is to remove the excess focus terms, get the model in better agreement with the observations on intended Zernike functions and produce a stronger signal. We may also have to use another basis besides Zernike functions, such as Laguarre-Gauss functions. We are using a Gaussian profile beam to probe the optic, which dies off rapidly at the edges of the optic. Zernike functions always come to a minimum or maximum at the edge of the unit circle, whereas Laguarre-Gauss functions die off at the edges, just like our beam.

Our results seem to indicate that with these changes, a closed-loop system which can flatten the peak to valley optical path distortion to within $1nm$ can be created.

.1 Selected Zernike Functions

N	n	m	Zernike Polynomial	Rectangular Representation	Common name
1	0	0	1	1	Piston
2	1	0	$\rho \sin \theta$	x	Tilt about y axis
3	1	1	$\rho \cos \theta$	y	Tilt about x axis
4	2	0	$\rho^2 \sin 2\theta$	$2xy$	Astigmatism with 45° axis
5	2	1	$2\rho^2 - 1$	$2x^2 + 2y^2 - 1$	Focus
6	2	2	$\rho^2 \cos 2\theta$	$y^2 - x^2$	Astigmatism with 90° axis
7	3	0	$\rho^3 \sin 3\theta$	$3xy^2 - x^3$	Triangular astigmatism with base along x-axis
8	3	1	$(3\rho^3 - 2\rho) \sin \theta$	$3x^3 + 3xy^2 - 2x$	Third order coma along x-axis
9	3	2	$(3\rho^3 - 2\rho) \cos \theta$	$3y^3 + 3x^2y - 2y$	Third order coma along y-axis
10	3	3	$\rho^3 \cos 3\theta$	$y^3 - 3x^2y$	Triangular astigmatism with base along y-axis
11	4	0	$\rho^4 \sin 4\theta$	$4y^3x - 4x^3y$	
12	4	1	$(4\rho^4 - 3\rho^2) \sin 2\theta$	$8x^3y + 8y^3x - 6xy$	
13	4	2	$6\rho^4 - 6\rho^2 + 1$	$6x^4 + 6y^4 + 12x^2y^2 - 6x^2 - 6y^2 + 1$	Third order spherical aberration
14	4	3	$(4\rho^4 - 3\rho^2) \cos 2\theta$	$4y^4 - 4x^4 + 3x^2 - 3y^2$	
15	4	4	$\rho^4 \cos 4\theta$	$y^4 - 6x^2y^2 + x^4$	

Table 1: The first 15 Zernike Functions

.2 LabView Control VI Explanation

Overview of LabView Virtual Instrument

Name - AOMGalvoControl.VI

Sub VI's you need for AOMGalvoControl.VI to work: numbercrunch.vi, matrix-maker.vi, powerscramble.vi, rampedsine.vi, simplesine.vi.

Function - This virtual instrument is used to control the dynamic thermally adaptive optics experiment. Specifically, it takes the power matrix provided by the model of the optic as well as the galvo control parameters on the front panel of the VI and scans the laser across the face of the optic with the appropriate power at each location. The laser, AOM driver and galvos must be turned on manually. The power matrix must be written to a file at the specified location: E:/Program Files/National Instruments/

LabVIEW/AOMGalvoControl/aomvolt.txt in order for the vi to work properly.

I. AOMGalvoControl.vi - the main vi

This vi is located on boletus.mit.edu at E:/Program Files/National Instruments/LabVIEW/AOMGalvoControl/AOMGalvoControl.vi.

1. The front panel

When the vi is opened, the top portion of the control panel, which should be enough to operate the vi, will be in view. If you scroll very far down, there are more controls which should not be tampered with unless you know what you are doing. Objects in the front panel are distinctly colored to distinguish controls and indicators from one another.

(a) Top portion of control panel These will be the controls you will use most frequently to run the galvos and the AOM.

i. On/off control

This must be in the "on" position for the vi to run. If the vi is running, it terminates the program and sets voltages at all channels equal to zero when set to "off". If it is set to "off" and the vi doesn't stop

running, stop it with the control menu; the vi is waiting for an update and terminating it during this process will cause no harm. The switch snaps into place, so it stays either "on" or "off" without a preferred default.

ii. Output channels

The output channels are clearly marked on the front panel. Channel 0 controls the Y galvos, channel 1 controls the X galvos, channel 2 controls the AOM driver (intensity modulation) and channel 3 sends periodic 10 volt TTL signals to the wavefront sensor.

iii. X/Y radial step size

This controls the size of the X/Y radial step IN MILLIMETERS.

iv. X/Y number of radial steps

This controls the number of radial steps INCLUDING the center point.

v. X/Y maximum amplitude

This indicates the maximum distance of the beam from the center point when it is on the outmost ring. It is measured in CENTIMETERS. A formula for this quantity is below the panel, expressed in terms of the other controls on the front panel.

vi. Update rate

Use this control to regulate the speed of the scanning pattern. KEEP THIS HIGH IF POSSIBLE. Built in pauses in the scanning pattern (for the purpose of updating the WFS input) stop the galvos where they were while the computer updates the power matrix, then start scanning again at the center, RATHER THAN PICKING UP WHERE IT LEFT OFF. So interior points will get heated slightly more than outer ones in closed loop tests, and a high update rate will minimize this effect because it limits the amount of energy deposited at each individual point.

vii. # of revolutions at each radial setting

This controls the number of times the laser sweeps out a circle of a given radius before moving on to the next radius. This is normally set to 1, and is determined by the model of the optic. Do not use it to regulate scanning speed.

viii. Points per revolution

This controls the number of angular points for each given circle. This is usually determined by the model and should not be used to regulate the scanning speed.

ix. Actual waveform frequency

This indicates what frequency (in cycles per second, where a cycle is one circle) the galvos move at. Notice that if you tell it to trace out each circle N times, the frequency is divided by N: a cycle corresponds to how long the galvos dwell at one given radius.

x. Matlab wait

In the idealized closed loop system, time is needed for Matlab to decompose the WFS input into its Zernike components and produce a voltage matrix for the AOM. The time it takes Matlab to do this WHILE THE VI IS RUNNING (things run slower when the vi is operating) must be estimated and put here. Set it to 1 when performing open loop tests. This causes a brief (millisecond or so) pause in the scanning pattern, after which the pattern RESUMES AT THE CENTER.

xi. Wavefront update time

This controls how often you update your system in a closed loop test, and is usually set to around 10 minutes. In an open loop test, keep it larger than the time you intend to let the optic heat, as it introduces a pause in the scanning pattern, after which it RESUMES IN THE CENTER. If it does this often during an open loop test, you will get asymmetric heating, with more near the center points.

xii. Total number of points, X/Y

This gives the total number of points in the scanning grid.

(b) Bottom portion of the control panel

DO NOT TOUCH THESE UNLESS YOU KNOW WHAT YOU ARE DOING. These controls will probably remain the same no matter what experiment you are doing.

i. Channels

Controls what channels the y galvo, x galvo and aom voltages go to, respectively. The assignment of channel 3 to the TTL signal is made inside the vi diagram.

ii. X/Y phase

The generating function for the scanning pattern is a sine wave. The phase determines what shape the scanning pattern makes. This vi was designed to have X as a cosine (phase=.5) and Y as a negative sine (phase=1.0).

iii. X/Y dc offset

This puts a dc voltage offset to the galvos. It isn't calibrated to correspond to a linear distance.

iv. X/Y galvo calibration factor

This is a "fudge factor" for galvo calibration. The beam alignment on the optic must be done manually, and this calibration factor, along with the offsets, must be used to center the beam on the optic as well as to make sure the outer circle of the scanning grid is on the edge of the optic.

v. File path to get AOM voltage matrix

This tells Labview where to look in order to get the AOM voltage matrix (corrisponds to the power matrix). Don't change this unless you have Matlab put the output file in the proper place. The conversion from the power matrix to input voltages to the AOM must be done outside of LabView.

2. The wiring diagram for AOMGalvoControl.vi

The wiring diagram contains a nest of for, while, case and sequence loops. This description will start from the outside in. Sub vi's will be mentioned, but they will be explained in further detail in their own sections.

(a) The outer-most sequence

All components of the vi except for the "Matlab wait" control are encased in this. "Matlab wait" is the only number used in more than one frame of the outer-most sequence.

i. Frame zero of the outer-most sequence

This frame contains only two components: a TTL signal of 10 volts being sent out by channel 3 (to trigger the wavefront sensor) and a 1 millisecond wait, to fix the duration of the pulse.

ii. Frame one of the outer-most sequence

This frame contains only two components: a function setting the voltage of channel 3 to zero (ending the TTL pulse), and a wait corresponding to the time entered in the "Matlab Wait" control. This wait is designed to let Matlab determine the first power matrix and save it to a file before LabView looks for it.

iii. Frame three of the outer-most sequence

This frame is listed out of order because like the previous two and unlike the next one, it is simple. It merely sets channels 0,1,2,3 to zero. All channels will go to zero if the vi is properly shut down (with the on/off switch on the front panel).

iv. Frame two of the outer-most sequence

This is the frame which does all of the work. It has a while loop enclosing everything in this frame, which is terminated by the "on/off" switch. This while loop keeps the inner-most sequence cycling through all of its frames.

(b) The inner-most sequence

This sequence lies in frame two of the outer-most sequence, as well as the largest while loop. Almost all of the terminals corresponding to the controls on the front panel lie outside of it, as they are used in more than one frame of the inner-most sequence.

i. Frame zero of the inner-most sequence.

This frame of the inner-most sequence, along with frame three of the inner-most sequence, do most of the work in this vi. The purpose of this frame is to control the galvos and the AOM until the wavefront update time (usually about 10 minutes) has expired, at which time it moves on to the next few frames, which trigger the WFS. I will describe this frame from left to right, roughly following the order which LabView executes the chain which controls the galvos and AOM.

A. Number Cruncher - sub vi

The majority of the terminals from the controls on the front panel lead into both copies of this sub-vi. Some information leaves and is fed into the Ramped Sine sub-vi. There are two of this vi, one for each galvo. See further down in this document for a more detailed description of this vi.

B. Ramped Sine - sub vi

This sub-vi takes inputs from the Number Cruncher sub-vi as well as some of the terminals connected to controls on the front panel. The output of this sub-vi is an array with elements corresponding to *UNSCALED* voltages sent to either the X or the Y galvo. The result must be divided by the X or Y galvo calibration factor, which is determined from an independant calibration for your experiment, and then entered in the control in the lower portion of the front panel. See further down in this document for a more detailed description of this vi.

C. Matrix Maker - sub vi

This sub-vi takes inputs from BOTH of the Ramped Sine sub-vi

and outputs to the AO write command. The output of this sub-vi is an array containing a complete instruction book for the galvos and aom; it has all of the voltages for channels 0,1 and 2. The voltages for channels 0 and 1 are duplicated and the voltages for channel 2 are alternate between zero and the actual aom voltage - this turns the beam off between points as it sweeps to the next one. See further down in this document for a more detailed description of this vi.

D. The channel output chain

This chain starts with the AO config command, moves on to AO write, AO start and finally to the inner-most for loop. It only takes the total number of points, the update rate and the channels from the front panel as inputs.

E. The inner-most for loop

This for loop is what causes the pattern to cycle endlessly unless the "on/off" switch is flipped or if it has exceeded the amount of time allotted in the "wavefront update time" control. If it stops because of the latter, only a brief pause ensues before the inner-most frame moves forward to another frame which looks similar to this one and the scanning of the laser begins again. It contains a AO write command which continuously outputs voltages to channels 0,1 and 2. The other components cause the loop to terminate after the time has expired, if there is an error with LabView or if the "on/off" switch is set to the off position.

F. AO 1-UP

The three AO 1-UP commands in the right of the inner-most sequence resets channels 0,1 and 2 to a voltage of zero. This ensures that no power is hitting the optic during the brief delay during which LabView triggers the WFS.

ii. Frame one of the inner-most sequence

This frame does only two things: sends a 10V TTL signal to channel 3, and has a 1 millisecond wait. The purpose of this and the next frame is to trigger the WFS in the middle of the scanning run, allowing it to take take images of the wavefront for use in the next iteration fo the servo loop.

iii. Frame two of the inner-most sequence

This frame does one thing: restores the voltage at channel 3 to zero.

iv. Frame three of the inner-most sequence

This frame performs the same function as frame zero of the inner-most sequence, except that the time limitation is not how long the optic takes to respond to the heating, but rather how long it takes the WFS to take and average data, and how long it takes Matlab to take the wavefront and produce a usable text file containing the voltages going to the AOM (equivalent to a power matrix). The time limit on this frame is set by the Matlab Wait Time control on the front panel.

II. Number Cruncher

Number Cruncher serves primarily to neaten up the diagram for AOMGalvoControl.vi. It performs numeric math on scalars only. The label on it says "# crch".

1. Inputs

(a) # of inner rings to skip

This used to allow the user of AOMGalvoControl.vi to specify how many center rings to skip in the scanning pattern. However, modifications were made to a model we used, and we had to use the center point. This proved difficult to do because the original vi would have repeated the center point in the scanning pattern a number of times equal to the number of points per revolution in the outer circles. As a result, changes were made to SimpleSine.vi, the most basic component of AOMGalvoControl.vi, so that a single zero point was always included. As a result, the option to skip the

center point no longer exists, and the # of rings to skip now has a constant of 0 being fed to it.

- (b) Number of steps, step size, number of revolutions, points per revolution
These have been explained in the front panel section of AOMGalvoControl.vi.

2. Outputs

- (a) Maximum amplitude

This outputs the radius of the outermost ring in the scanning pattern.

- (b) Buffer size

This is the number of points of a single cycle, times four. A factor of two is acquired when the galvos circle inward rather than outward, and another is acquired when each element of the X and Y galvo arrays is duplicated in order to allow the AOM to turn on and off at each point. It is fed into the Buffer Size terminal on AO Config.

- (c) Buffer length

This is "points per revolution" on the front panel of AOMGalvoControl.vi. It is fed into the Buffer Length terminal for RampedSine.vi.

- (d) Cycles in buffer

This is "number of revolutions" on the front panel of AOMGalvoControl.vi. It is fed into the Cycles in Buffer terminal for RampedSine.vi.

- (e) Initial amplitude

This is now always zero, since the center point is always included.

- (f) Step size, number of steps, total number of points

This is explained in the front panel section for AOMGalvoControl.vi.

III. Ramped Sine

Ramped Sine produces an array with the points over which the X and Y galvos will scan. The output is not calibrated; one has to set the dc offset and the calibration

factor on the lower portion of the front panel of AOMGalvoControl.vi in order to get the proper voltages to be sent to AO Write. It is this vi which combines an inwards and outwards scanning pattern to get a smooth, clockwise, repeating pattern that goes out and in. It uses SimpleSine.vi with a varying amplitude to create the pattern. All inputs and outputs to this VI have been explained in other sections. The label on it says "ramp sine 1".

IV. Simple Sine

Simple Sine produces a simple sine wave which Ramped Sine modifies to make the scanning voltages for the galvos. It uses a case loop so that the center point is included only once rather than multiple times for each angular point along a circle. All inputs and outputs have been explained elsewhere. The label on this VI reads "Simp Sine".

V. Matrix Maker

Matrix Maker takes the array with the points on the scanning pattern from RampedSine.vi as well as the AOM voltage array from PowerScramble.vi (a sub-vi of MatrixMaker.vi) and splices them together. It rearranges X and Y galvo arrays so that each element repeats. However, the AOM voltage array from PowerScramble.vi already has zeros inserted between each element. The results are combined into the output which is fed to AO Write. All inputs and outputs for this VI have been explained elsewhere. It has a label which reads "Array Make".

VI. Power Scramble

Power Scramble opens the file located at E:/Program Files/National Instruments/LabVIEW/AOMGalvoControl/aomvolt.txt, doubles it over (for the inward-then-outward scanning pattern) in the same fashion that RampedSine.vi doubles over the X and Y galvo arrays, and inserts a zero in between each element (where a zero corresponds to the laser being shut off between scanning points). The output is read by MatrixMaker.vi. All inputs and outputs of this VI have been explained elsewhere. This VI has a label which reads "pwr scl".

.3 Data

Figure -1: Wavefront form of $N = 4, 5, 8$ and 10

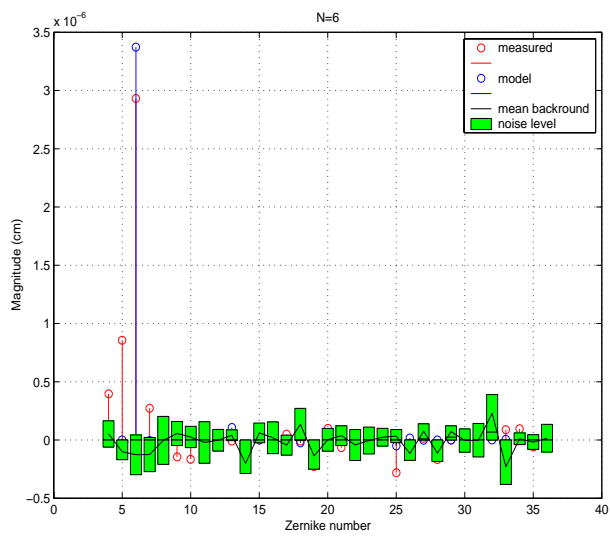
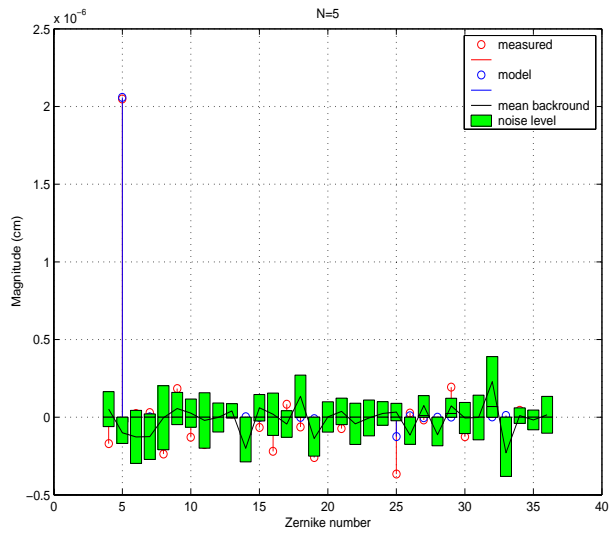
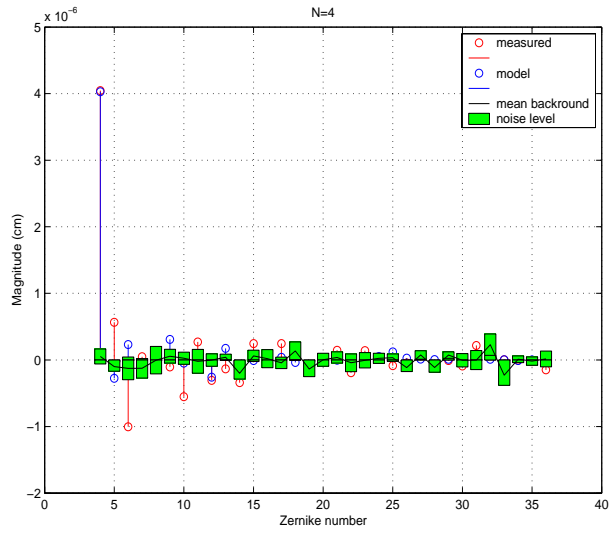


Figure -2: Data for $N = 4, 5$ and 6

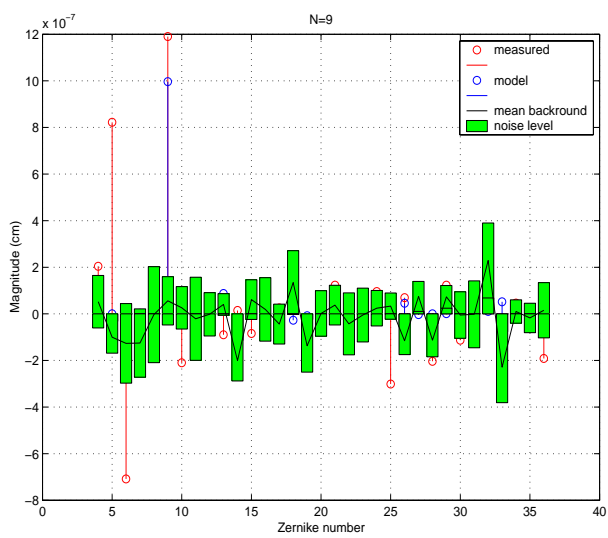
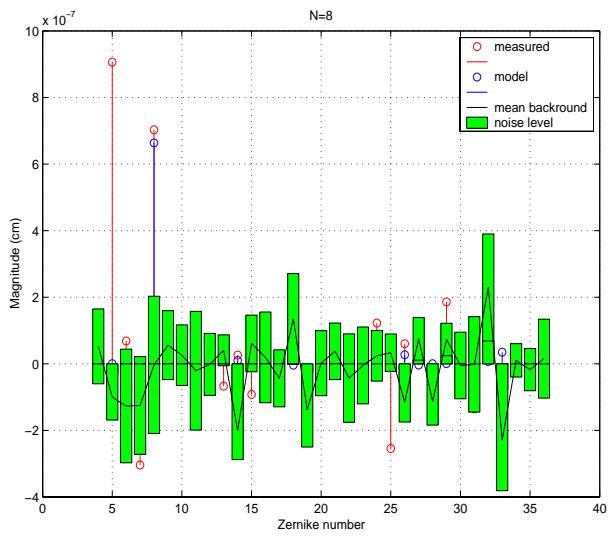
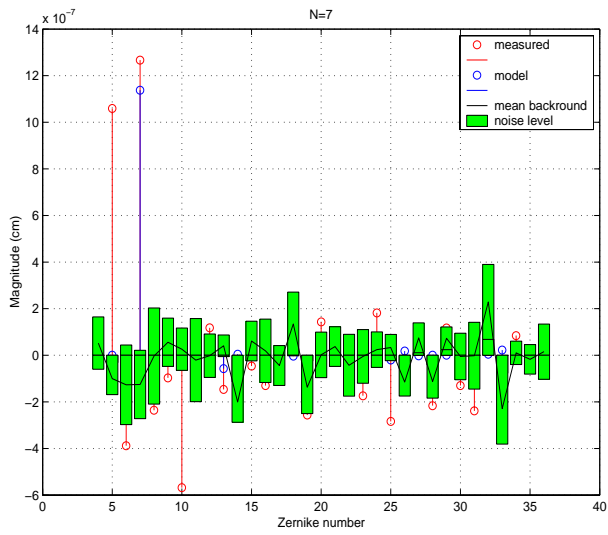


Figure -3: Data for $N = 7, 8$ and 9

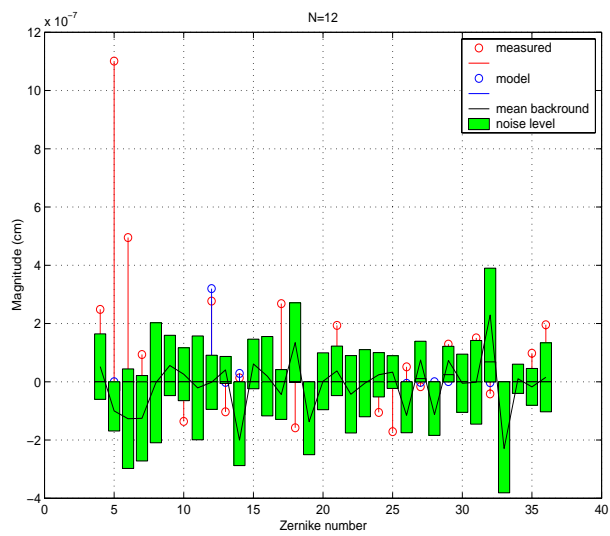
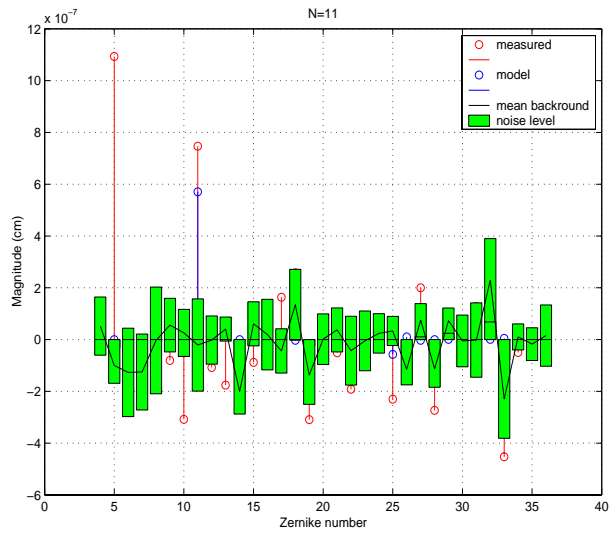
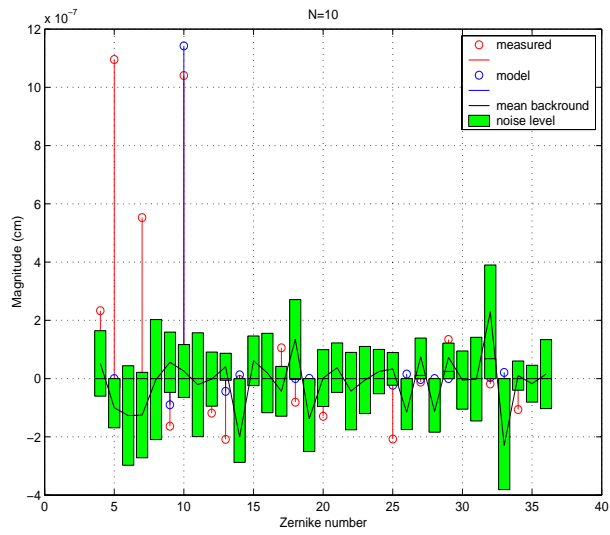


Figure -4: Data for $N = 10, 11$ and 12

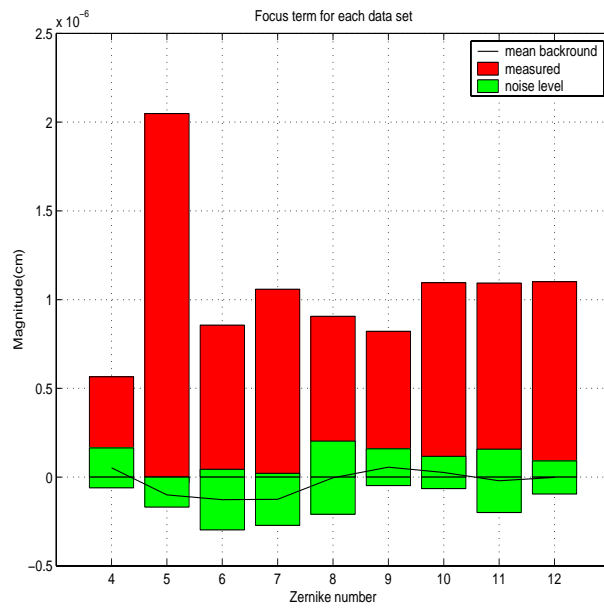
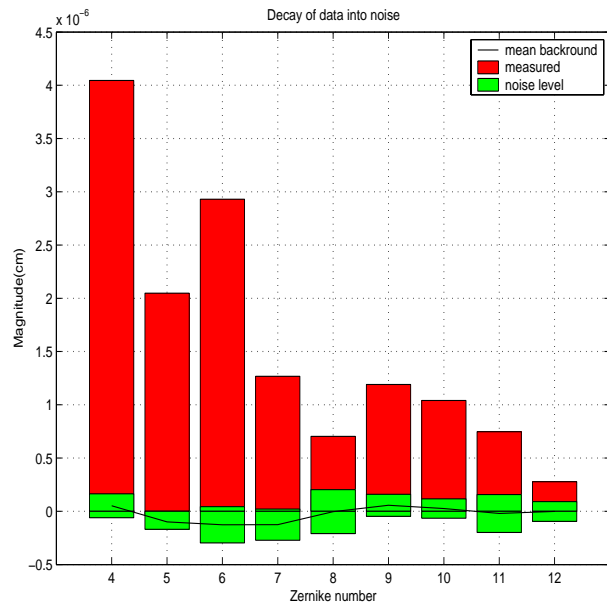


Figure -5: Data figures

Bibliography

- [1] Robert Bennett, *Thermally Adaptive Optics in LIGO II*. B. S. thesis, Massachusetts Institute of Technology (2000).
- [2] Brett Bochner, *Modelling the Performance of Interferometric Gravitational-Wave Detectors with Realistically Imperfect Optics*. Ph. D. thesis, Massachusetts Institute of Technology (1998).
- [3] Brian Thomas Lantz, *Quantum Limited Optical Phase Detection in a High Power Suspended Interferometer*. Ph. D. thesis, Massachusetts of Technology (1999).
- [4] Ryan Lawrence, 2001, private communication. Gives explanation of dynamic thermal compensation theory. Provided experimental setup figure.
- [5] Malacara, Daniel, Optical Shop Testing. New York, NY: John Wiley & Sons, Inc., 1978.
- [6] Nergis Mavalvala, *Alignment Issues in Laser Interferometric Gravitational-Wave Detectors*. Ph. D. thesis, Massachusetts Institute of Technology (1997).
- [7] Megan Owens, 2001, private communication. Provided Fabry-Perot/delay-line interferometer figure.
- [8] J. G. Rollins, *The Search for Gravitational Radiation with Laser Interferometers and Improvements to the LIGO 40-meter Laboratory*. B. S. thesis, University of Michigan (1999).
- [9] Saulson, Peter R., Fundamentals of Interferometric Gravitational Wave Detectors. River Edge, NJ: World Scientific Publishing Co., 1994.

[10] Rainer Weiss, 2001, private communication.